

# Microwave View on Particle Acceleration in Flares

Gregory D. FLEISHMAN

*Physics Dept., New Jersey Institute of Technology, Newark, NJ 07102 USA  
Central Astronomical Observatory at Pulkovo of RAS, Saint-Petersburg 196140, Russia*

(Received 2013 March 24; accepted 2013 March 31)

## Abstract

Although the solar flare phenomenon is widely accepted to be a consequence of release of excessive magnetic energy stored in the coronal currents (stated another way—in nonpotential magnetic fields), many essential details of this energy release remain poorly understood. Initially, the released flare energy is somehow divided between thermal and nonthermal components through plasma heating and particle acceleration, respectively, although this proportion can then change in the course of the flare due, e.g., to fast particle Coulomb losses leading to additional plasma heating and/or chromospheric evaporation. So far, the thermal-to-nonthermal partition was found to vary greatly from one flare to another resulting in a broad variety of cases from ‘heating without acceleration’ (Battaglia et al. 2009) to ‘acceleration without heating’ (Fleishman et al. 2011). Recent analysis of microwave data of these differing cases suggests that a similar acceleration mechanism, forming a power-law nonthermal tail up to a few MeV or even higher, operates in all the cases. However, the level of this nonthermal spectrum compared to the original thermal distribution differs significantly from one case to another, implying a highly different thermal-to-nonthermal energy partition in various cases. This further requires a specific mechanism capable of extracting the charged particles from the thermal pool and supplying them to a bulk acceleration process to operate in flares *in addition* to the bulk acceleration process itself, which, in contrast, efficiently accelerates the seed particles, while cannot accelerate the thermal particles. Within this ‘microwave’ view on the flare energy partition and particle acceleration I present a few contrasting examples of acceleration regions detected with microwave data and compare them with the most popular acceleration mechanisms—in DC fields, in collapsing traps, and stochastic acceleration by a turbulence spectrum—to identify the key elements needed to conform with observations. In particular, I point out that the turbulence needed to drive the particle acceleration is generated in nonpotential magnetic structures, which results in nonzero helicity of the turbulence. This helicity, in its turn, produces a nonzero mean DC electric field on top of stochastic turbulent fields driving the main stochastic acceleration; thus, acceleration by helical turbulence combines properties of the standard stochastic acceleration with some features of acceleration in DC electric fields, exactly what is demanded by observation.

**Key words:** acceleration of particles—instabilities—radiation mechanisms:non-thermal—Sun:flares—Sun:radio radiation

## 1. Introduction

Microwave continuum radio bursts are believed to be primarily produced by an electron population magnetically trapped near the top of a flaring magnetic loop rather than the accelerated electron component directly (Lee et al. 1994; Melnikov 1994; Kundu et al. 2001; Melnikov et al. 2002). Using the radio emission produced by this trapped electrons for diagnostics of the particle acceleration is difficult because this task requires to disentangle effects of acceleration and transport, which is expected to be model dependent. Although some exciting results have been obtained in this way (see, e.g., Reznikova et al. 2009), it is yet unclear how unique they are. The most recent developments in this area are discussed in Melnikov’s article in this proceeding volume, so I am not going to discuss the particle transport outside the acceleration region in any detail.

To outline the framework of the further discussion we

emphasize that the GS continuum radio emission can be produced by any of (i) a magnetically trapped component or (ii) a precipitating component, or (iii) the primary component within the acceleration region, rather than exclusively by the magnetically trapped component. What is highly important for diagnostics, these three populations of fast electrons produce radio emission with distinctly different characteristics (Fleishman et al. 2011). Indeed, in the case of magnetic trapping the electrons are accumulated at the looptop (Melnikov et al. 2002), and the radio light curves must be delayed by roughly the trapping time relative to accelerator/X-ray light curves. In the case of radio emission from the acceleration region, even though the residence time that fast electrons spend in the acceleration region can be relatively long, the radio and X-ray light curves are proportional to each other simply because the flux of the X-ray producing electrons is equivalent to the electron loss rate from the acceleration region.

Therefore, what is needed to study the acceleration re-

gion in the microwave domain is to cleanly separate its contribution from the two other mentioned competing contributions—from the magnetically trapped and precipitating components. Note that having imaging spectroscopy observations this separation will be routinely possible for many events. Meanwhile, however, we are limited to some favorable cases when either no magnetic trapping takes place or the acceleration region contribution dominates temporarily or/and spectrally over the competing contributions. Below we review a few such favorable cases and discuss the obtained acceleration region properties vs available mechanisms of particle acceleration.

Main acceleration mechanisms that can play a role in solar flares include both regular and stochastic processes. Regular energy gain can take place in a DC electric field or in a contracting source (e.g., collapsing magnetic trap), while the stochastic acceleration can be driven by turbulence either resonantly (the case of short-wave turbulence) or nonresonantly (large-scale turbulent pulsations). There can be processes combining some regular and stochastic features—e.g., diffusive shock acceleration, while acceleration by an ensemble of shock waves represents a special example of stochastic acceleration (for general overview of the acceleration processes see, e.g., Fleishman & Toptygin 2013a). Importantly, predicted observational manifestations of all these acceleration mechanisms are different from each other (Li & Fleishman 2009; Park & Fleishman 2010), which implies that they can be distinguished observationally.

## 2. Cold, dense flare: acceleration with mild heating

Bastian et al. (2007) analyzed Yokohoh and GOES X-ray data together with Nobeyama and OVSA radio observations to describe a new class of ‘cold flares’—flares that occur in such dense coronal magnetic loops that the flare energy deposition is insufficient to substantially heat the coronal plasma, even though most of the flare energy is deposited in the coronal rather than the chromospheric part of the dense loop.

A ‘textbook’ example of this class of events was the solar flare occurred on 2001 October 24 in NOAA active region 9672 at a heliocentric position of S18W13 from approximately 23:10–23:14 UT. A strong radio burst was well-observed in total intensity by OVSA, NoRP, and NoRH allowing a detailed analysis of the event. A puzzling feature of this flare is that no soft X-ray emission was noted by NOAA/SEC from the event, although weak extreme-ultraviolet (EUV), soft X-ray (SXR), and hard X-ray (HXR) emissions were detected from the flare by the *Transition Region and Coronal Explorer* (TRACE; Handy et al. 1999), the *Yohkoh* Soft X-ray Telescope (SXT), and Hard X-ray Telescope (HXT), respectively (Kosugi et al. 1992), as was a weak SXR enhancement by the GOES 10 satellite.

Thus, the microwave data is the main source of information for this event. Fig. 1a,b shows the 17 and 34 GHz maps in total intensity (Stokes I) near the time of the

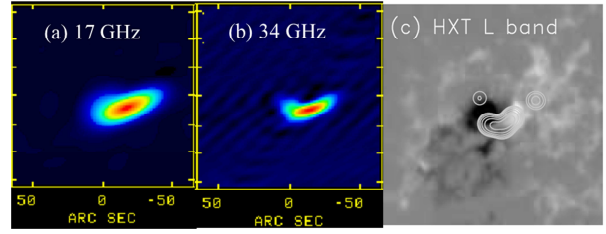


**Fig. 1.** Flare images and the Kitt Peak magnetogram. a,b) The images of the 17 and 34 GHz total intensity at the time of 17 GHz flux maximum. c) HXT L band map on top of the Kitt Peak magnetogram.

emission maximum. The source morphology evolves very little at radio wavelengths as a function of time. The peak brightness temperature of the 17 GHz source is  $4.6 \times 10^7$  K whereas that of the 34 GHz source is  $1.8 \times 10^7$  K. Fig. 1c shows the HXR source in HXT/Yohkoh L band superposed on the magnetogram. The source in the SXR (not shown for brevity), HXR, and radio bands are coincident and quite similar in morphology, therefore, all imaging data are consistent with the illumination of a simple dense magnetic loop. The loop is not visible in the NoRH 17 and 34 GHz maps as a discrete feature in the active region prior to the flare; the estimate of the 17 GHz brightness temperature prior to the flare is  $\lesssim 10^5$  K.

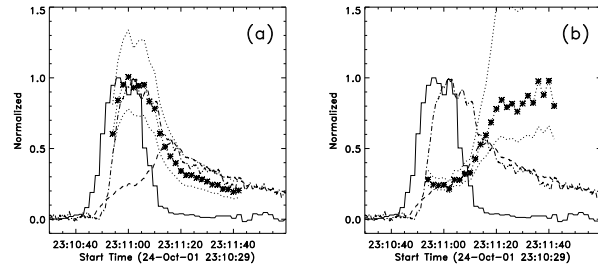


**Fig. 2.** The variation of  $n_{rl}$  and  $T$  with time derived from the fits in comparison to the HXR (solid line) and radio emission at 9.4 (dashed line) and 17 GHz (dash-dotted line). a) The asterisks show the variation of fitted value of  $n_{rl}$  (divided by  $10^7 \text{ cm}^{-3}$ ) for an assumed magnetic field of 165 G in the source. The dotted lines above and below this line are the corresponding values for the magnetic field strengths of 150 and 180 G, respectively. b) The corresponding plot for the temperature  $T$  variations (normalized by 6 MK) for the same assumption.

The spectrum of the radio emission with a sharp cutoff in the emission below  $\approx 10$  GHz, while a hard slope above  $\approx 20$  GHz, is clearly nonthermal, yet the brightness temperature of the 17 and 34 GHz sources is unexceptional, characteristic of optically thin gyrosynchrotron emission. It is reasonable to conclude that the low frequency cutoff is the result of the Razin effect, which strongly suppresses the gyrosynchrotron emission in the presence of an ambient plasma below a cutoff frequency  $\nu_R \approx 20n_e/B_\perp$ , where  $n_e$  is the thermal electron density and  $B_\perp$  is the perpendicular component of the magnetic field vector in the source relative to the line of sight. For  $\nu_R \sim 10 - 15$  GHz, a mag-

netic field strength of  $\sim 150 - 200$  G at an angle  $\theta = 60^\circ$  to the line of site implies the density is  $n_e \sim 10^{11} \text{ cm}^{-3}$ . Higher magnetic fields imply higher densities.

Estimate of the free-free optical depth at radio wavelengths shows that if Razin suppression is important, free-free absorption is, too. Bastian et al. (2007) concluded that a combination of *Razin suppression* and *free-free absorption* plays a role in determining the shape of the radio spectrum.

Bastian et al. (2007) applied a nonlinear model-fitting code that adjusts model parameters to minimize the  $\chi^2$  statistic using the downhill simplex method (Press et al. 1986). They fit the model to 25 composite radio spectra observed by OVSA (5-14.8 GHz) and the NoRP (9.4, 17, 35, and 80 GHz), as indicated in Fig. 2.

A uniform source model with an area  $A = 2 \times 10^{18} \text{ cm}^2$  ( $12'' \times 30''$ ) and a depth  $L = 9 \times 10^8 \text{ cm}$  ( $12''$ ), consistent with the X-ray and radio imaging was used. The source volume is assumed to contain thermal background plasma with a density  $n_{th}$  and a temperature  $T$ . The source is assumed to be permeated by a coronal magnetic field  $B$  with an angle  $\theta$  relative to the line of sight. A power-law distribution of energetic electrons  $N(E)dE = KE^{-\delta}dE$  is assumed, with a normalization energy  $E_o$  and a high-edge cutoff energy  $E_c$ . The total number density of energetic electrons between  $E_o$  and  $E_c$  is  $n_{rl}$ .

Fig. 2 shows a comparison between the fitted values for  $n_{rl}$  and  $T$  and the radio and HXR emission as a function of time for a magnetic field of 165 G. Two points can be made about the apparent trends: 1) the total number of energetic electrons tracks the variation of the radio emission. The maximum of the  $n_{rl}$  is coincident (to within 2 s) to the 35 GHz flux maximum; 2) the temperature of the ambient plasma increases with time. With  $B = 165$  G,  $T$  increases from  $\sim 1 - 2 \times 10^6$  K to only  $\sim 4 - 6 \times 10^6$  K. This manifests a discovery of a new class of flares, which occur in relatively compact cool and dense loop, giving rise to efficient acceleration of relativistic electrons and strong microwave emission, although to only a moderate plasma heating and very weak X-ray emission.

Nevertheless, the modest coronal plasma heating can be sensitively measured via a corresponding decrease of the free-free radio opacity of the flaring plasma. This permits a precise calorimetry of the flare energy deposited into nonthermal electrons and dissipated in the corona to heat the ambient plasma. From this analysis we found that the ratio of total energy of the nonthermal electrons in this flare was comparable to ( $\sim 30\%$  of) the magnetic energy of the flaring loop. The conclusion that the accelerated electron energy is about a few tens percent of the flare energy is consistent with recent RHESSI results (Brown et al. 2007) on the nonthermal flare energy budget.

Bastian et al. (2007) analyzed the decay phase of the radio light curves and found that the exponential decay constants did not depend on the frequency, which means that the particle escape time did not depend on the particle energy. Such an energy-independent particle transport implies that the transport was mediated by turbulence rather than the Coulomb collisions; it is the tur-

bulence that could drive stochastic electron acceleration at the impulsive phase of the flare. Note, that an interesting property of this transport/acceleration regime is the observationally-proven *independence* of the *electron escape time on energy*.

### 3. Cold, tenuous flare: acceleration without heating

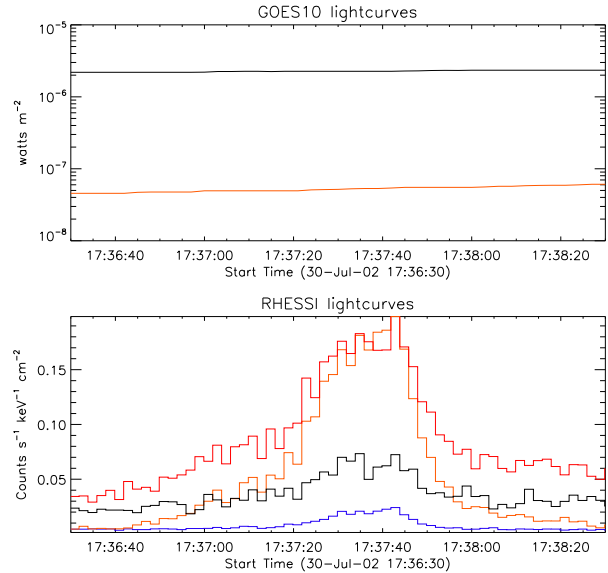


**Fig. 3.** 2002 July 30 flare: GOES (3 s; upper panel) and RHESSI (2 second bins) lightcurves (bottom panel) in: 3-9 keV (black), 9-15 keV (red), 15-30 keV (orange), 30-100 keV (blue).

Another vivid example illustrating the unique capacity of microwave observations is a cold, tenuous flares (RHESSI nugget No. 153)—which allowed detection and study of the very acceleration region of fast electrons in the flare. The unusual nature of this event is immediately apparent in Fig. 3. There is a nice RHESSI hard X-ray burst of about one minute duration, with count rates like those typically seen in M-class flares, but remarkably there was no counterpart visible at all (less than the GOES C1 level) in soft X-rays. The location and morphology of the event are also interesting. Fig. 4 shows that it occurred in the following portion of the active region. In this figure the green arc in the right panel shows a magnetic loop identified at the correct location in the extrapolated magnetic model. The three bands shown in the left panel are 9-15 (red), 15-30 (orange), and 30-100 keV (blue). Note the lack of a looptop source at any point in the event—the footpoint structures extend to remarkably low (9-15 keV) energy. It is otherwise the classical morphology of a coronal flux bundle, with a length inferred to be some  $4 \times 10^9 \text{ cm}$  and volume  $6 \times 10^{26} \text{ cm}^3$ . These geometrical constraints, plus the diagnostic information obtained from the X-ray, radio, and magnetic observations, allow a great deal to be learned about this unusual flare; particularly, about the thermal/nonthermal energy partition with a strongly dominating nonthermal component, which

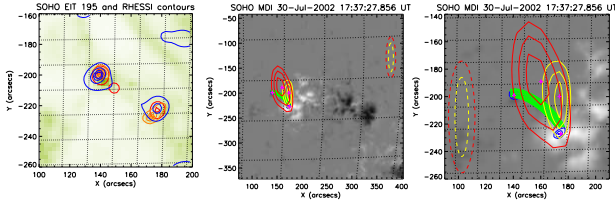


**Fig. 4.** Left: Spatial distribution of X-ray emission from 2002 July 30 flare in various energy ranges contours at 30, 50, 70, 90% levels: 9 – 15 keV (red) 15 – 30 keV (orange), 30 – 100 keV (blue). Background image is SoHO EIT 195 taken just before the flare at 17 : 36 UT. Middle and right: the full and close-up view of the active region and an extrapolated flux tube (green) connecting two X-ray footpoints (blue contours), 2.6 – 3.2 GHz radio image (red contours) and 4.2 – 8.2 GHz (yellow contours). Magenta plus signs mark the spatial peaks of the HXR and radio sources. Dashed ellipses display the sizes of the synthesized beams.

says something remarkable about the acceleration mechanism operating in this event. The microwave spectra offer further clues.

Fig. 5 includes some double-peaked microwave spectra fitted with two components of differing magnetic field strength, and shows the inferred number and number density time profiles of electrons involved in producing the observed radiation (lower panels). Fleishman et al. (2011) find that  $6 \times 10^{35}$  electrons above 6 keV are necessary, and that the density of these electrons approaches  $10^9 \text{ cm}^{-3}$ . This density, consistent with the RHESSI-derived acceleration rate for a fast-electron trapping time of 3 s, easily agrees with the low upper limit for the thermal plasma distribution in the loop, inferred from the lack of soft X-rays. Fleishman et al. (2011) conclude that the event was dominated by non-thermal plasma, with the main (low-frequency) component being due to the acceleration site itself, in a region of low magnetic field ( $\sim 60 \text{ G}$ ), while the second (high-frequency) component arises from the precipitation region of substantially higher magnetic field strength ( $\sim 370 \text{ G}$ ). Although the energetic electrons bombard the chromosphere at a rate comparable to that of an average GOES M-class flare as seen from RHESSI, the flare shows little evidence for significant thermal plasma heating or chromospheric evaporation. A highly asymmetric flaring loop, combined with rather low thermal electron density, have made it possible to detect the **GS radio emission** directly from the **acceleration site**. We appear to have here a clear case of a *thermally “cold” object dominated by nonthermal acceleration*: the electron distribution function in the coronal plasma consists mainly of fast particles, with no evidence for a comparably strong thermal signature. The physics of such an object is ill-understood at the present time but is consistent with a **stochastic acceleration mechanism** with a roughly *energy-independent lifetime* for the fast electrons in the acceleration region. This discovery, therefore, offers stringent new constraints on the acceleration mechanism in flares.

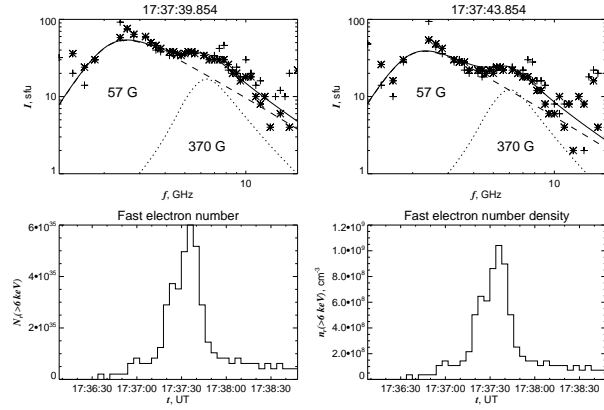


**Fig. 5.** OVSA radio spectra obtained by two small antennas (pluses and asterisks) and model GS emission from the acceleration region (dashed lines), precipitating electrons (dotted lines), and sum of these components (solid line). Total number and number density of the fast electrons at the radio source as derived from the OVSA radio spectrum.

#### 4. A normal, 11 Apr 2002, flare: mild acceleration with a significant heating

One more example, where the radio contribution from acceleration region dominates the low-frequency part of the microwave spectrum over a limited time is the 11 Apr 2002 flare; Fig. 6. The acceleration region contribution was identified with the impulsive peak from 16:20:00 to 16:20:20 UT based on analysis of images and light curves and confirmed by radio spectral fit, the results of which are shown in Fig. 6.

The derived evolution of the physical parameters deserves some discussion. The magnetic field in the low-frequency source is about 120 G during the impulsive phase of the radio burst, while it drops quickly to 30–50 G at the transition to the decay phase around 16:20:20 UT. Remarkably, this magnetic field change derived from the *spectral fit*, Figure 6, happens at the very same time as the  $10''$  shift of the *spatial brightness peak*, see Figure 7, left. This implies that it makes sense to distinguish between these two spatially distinct low-frequency sources—the very acceleration region (the early source, with  $B \sim 120 \text{ G}$ , producing the impulsive radio emission) and the classical looptop radio source (the later source, with  $B \sim 40 \text{ G}$ , producing the radio emission from magnetically trapped electrons over the decay phase) spatially coinciding with the HXR source.

**Acceleration region.** At the impulsive low-frequency source,  $\sim 16:20:00$ – $16:20:20 \text{ UT}$ , the thermal number density obtained from the radio fit is somewhat low,  $n_e \lesssim 2 \cdot 10^9 \text{ cm}^{-3}$ , implying that the radio source is located in the corona, not at a chromospheric footpoint, while the number of nonthermal electrons is consistent with the acceleration rate derived from the HXR data,  $(1 - 3) \cdot 10^{34} \text{ electron/s}$ , if they reside at the radio source for 2–4 s, which requires the strong diffusion transport mode. The radio derived electron spectral index does not display any significant departure from the HXR derived electron spectral index during this time interval. All these



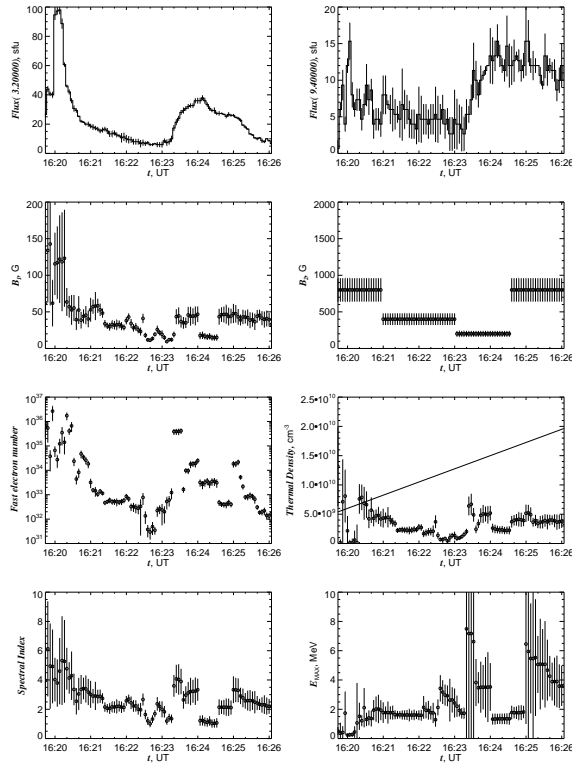


**Fig. 6.** Radio source parameters as derived from the OVSA spectral fit for five parameters of the low-frequency coronal source and adopted magnetic field value  $B_2$  for the ‘precipitating’ source as described in the text. A solid curve at the thermal plasma number density shows a number density evolution of the SXR source derived from emission measure from the RHESSI fit. Two top panels show the radio light curves recorded at 3.2 GHz and 9.4 GHz given for the reference purpose.

properties are similar to those determined for the acceleration site in the cold, tenuous flare discussed above, from which we conclude that we have here another instance of the acceleration region detection in a solar flare. The electrons accelerated at this source escape from there in roughly 3 s and then accumulate in another, ‘trapping’ source, which dominates the radio spectrum and spatial location after 16:20:20 UT. The acceleration, however, continues for a longer time: we note that the maximum electron energy,  $E_{\max}$ , displays a monotonic increase from  $\sim 300$  keV to  $\sim 2$  MeV over this phase of the burst ( $\sim 16:20:00$ – $16:20:50$  UT), which is reasonable to interpret as the growing of a power-law ‘tail’, i.e., the very process of the electron acceleration. Thus, the impulsive low-frequency source dominating the radio emission over roughly 16:20:00–16:20:20 UT, which produces fast electrons and supplies them to the coronal trapping site until at least 16:20:50 UT, can confidently be identified with the **acceleration region** of the flare under study.

**Electron accumulation site.** Transition to the gradual decay phase<sup>1</sup> at about 16:20:20 UT manifests the

<sup>1</sup> Its main parameters,  $B_1 \sim 30$ – $50$  G and  $n_e \lesssim 5 \cdot 10^9$  cm<sup>-3</sup>, clearly indicate its coronal location, although spatially distinct from the acceleration region showing a different coronal location.

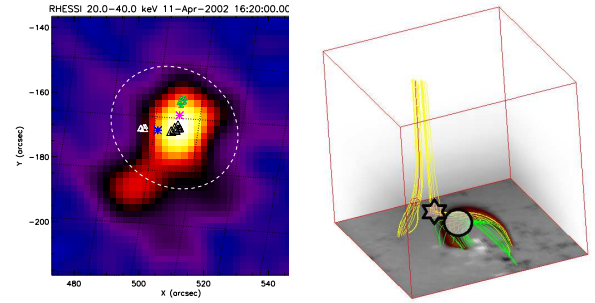


**Fig. 7.** Left: Evolution of the spatial brightness peak of the radio emission at 2.6–4.2 GHz from April 11, 2002 flare. Background: HXR image at 20–40 keV at 16:20:00–16:21:00 UT. Symbols are OVSA image centroid positions separated by 8 s time interval (OVSA temporal resolution for imaging): green triangles are for snapshots from 16:19:55 to 16:20:15 UT, pink asterisk for 16:20:20 UT, black triangles from 16:20:25 to 16:22:00 UT, white triangles from 16:23:40 to 16:24:20 UT, and the blue asterisk is for a late decay phase of 16:25:08 UT; larger triangles correspond to later snapshots within each group. The sequence of the contours clearly indicates that the radio source is located at the northern part of the HXR image and stays there during the entire impulsive phase, then moves southward to exactly match the HXR centroid position and stays there the entire decay phase of the first peak. The synthesized beam is shown by the dashed white oval. Right: 3D model of the flaring region based on LFFF extrapolation with  $\alpha \approx -5.5 \cdot 10^{-10}$  cm<sup>-1</sup> of the photospheric SOHO/MDI magnetogram visualized by two magnetic flux tube (central field lines are red): the first one consists mainly of the closed field lines (green) with a few outer open field lines (yellow), while the other one consists of open field lines only. The locations of the acceleration region and trapping source are shown on top of this structure by the star symbol filled with a semitransparent rose color and the circle filled with a semitransparent light grey color.

stage when the trapping site has accumulated a sufficient number of fast electrons to dominate the radio spectrum. At this time the derived number of accelerated electrons with  $E \gtrsim 20$  keV reaches a maximum of  $\sim 10^{36}$  electrons, which corresponds to the number density of the accelerated electrons of  $n_r \sim 2 \cdot 10^8$  cm<sup>-3</sup> for the adopted source volume. For the RHESSI-derived acceleration rate of  $(1-3) \cdot 10^{34}$  electron/s, having a total electron number of  $\sim 10^{36}$  requires a highly efficient electron trapping with the trapping time longer than 30 s. Indeed, that long trapping time is fully confirmed by the measured delay between the HXR/impulsive radio light curves and ‘non-impulsive’ radio light curves, some of which are delayed by almost one minute, see, e.g., the 1 GHz light curve in Figure 8, left.

The global parameters of the acceleration region determined from the spectral fit and imaging data are  $B \sim 120$  G and  $V \sim 6 \cdot 10^{27}$  cm<sup>-3</sup>, which are, respectively, two times and ten times larger than in the cold, tenuous (2002 July 30) flare (Fleishman et al. 2011). The residence time of the fast electrons at the acceleration region is  $\sim 3$  s, which is comparable to that in the cold, tenuous flare, and is much longer than the free-streaming time through the acceleration region. Again (Fleishman et al. 2011), this favors diffusive electron transport due to their scattering by turbulent waves and, thus, a stochastic acceleration

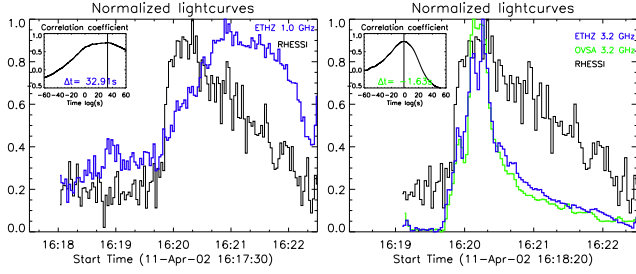


**Fig. 8.** Radio to HXR timing: RHESSI 20-40 keV light curve (black) and radio light curves at 1 GHz (left) and 3.2 GHz (right); as observed by Phoenix (blue) and OVSA (green). Insets show the lag-correlation results. For these two cases—non-impulsive light curve on the left and impulsive one on the right.

mechanism. The available data is, unfortunately, insufficient to firmly specify the version of stochastic acceleration mechanism (see, e.g., Petrosian 2012 or Fleishman & Toptygin 2013a for a recent review) operating in the event; however, it does favor those models predicting a roughly energy-independent diffusion time at the source, like in the cold flare event (Fleishman et al. 2011)

## 5. Early flare phase: heating-dominated energy release

In some flares the thermal component appears much earlier than the nonthermal component in X-ray range (Battaglia et al. 2009). Altyntsev et al. (2012) studied this ‘early flare phase’ using microwave observations from various instruments including NoRH, NoRP, SSRT, and RSTN. Their findings can be summarized as follows.

First of all, in all analyzed events there are nonthermal electrons that generate gyrosynchrotron emission at frequencies above the spectral peaks. In the case of power-law distribution of emitting electrons the best fit indices are in the range from 2.5 up to 4, with the high-energy cutoff above 1 MeV. The densities and energy contents of *nonthermal* components (i.e., above  $E_{cr} \sim 10 - 20$  keV, Fig. 9) were well below the *thermal* density and energy of the coronal sources.

Secondly, the thermal GS emission dominates the *low-frequency* microwave spectra in many cases. This offers reliable diagnostics of the source area and magnetic field. The radio estimate of the coronal source area is highly important because it is unbiased by the plasma density distribution, which is unlike the SXR-derived source area. The radio data clearly show that the source area grows at the course of the flare. This fully accounts for the observed increase of the SXR-derived emission measure, while no density increase is needed. This means that no essential chromospheric evaporation occurs in the analyzed cases, so no energy deposition to the chromosphere in the form of either precipitating electrons or heat conduction takes place. Since no energy transfer process is detected, the early flare phase sources are likely to represent the energy release and acceleration sites.

Thirdly, even though the thermal plasma contribution

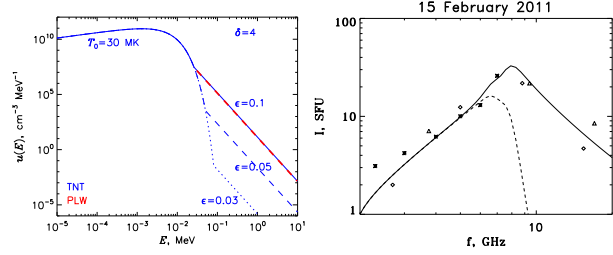


**Fig. 9.** Left: Thermal/nonthermal (TNT) electron distribution over kinetic energy (used to fit the radio spectrum in right panel) is shown for a few different  $\epsilon$  values. Right: observed microwave spectrum at the preflare phase of the 15 Feb 2011 flare as observed by NoRP, RSTN, and SSRT instruments. The best TNT fit (solid curve) and purely thermal fit (dashed curve) are superimposed on the observed data.

to the microwave spectrum is often essential, no purely thermal stage has been detected. Indeed, radio signatures of the nonthermal particles appear as soon as the plasma heating. Thus, the RHESSI (or Fermi) non-detection of the nonthermal emission at the early flare phase is accounted by its relatively low sensitivity, while the microwave observations turn out to be more sensitive to small numbers of the nonthermal electrons.

The plasma beta  $\beta$  is smaller than one, while the nonthermal energy density is much smaller than the thermal one in all the cases (i.e.,  $W_{nth} \ll W_{th} \ll W_B$ ). Although the total energy content of the accelerated electrons is small, the available nonthermal electrons are high efficiently accelerated from slightly nonthermal to relativistic energies. Their spectra are hard,  $\delta = 2.5 - 3$  in most cases, and extended up to a few MeV. Stated another way, the *shape* of accelerated particle spectrum at the preflare phase is similar to that during flares, even though their *levels* (normalizations) are highly different. This can happen, for example, if the same, presumably stochastic, acceleration mechanism capable of accelerating the charged particles from somehow created ‘seed population’ is involved at both preflare and flare phases. However, these seed populations must be formed differently in preflares or flares.

The observed significant plasma heating suggests that the corresponding flare energy is already available. However, it is divided highly unevenly between the plasma heating and nonthermal seed population creation. It works in a way similar to that in the presence of a DC electric field: at a preflare phase, a relatively large, but still essentially sub-Dreicer field, will heat the ambient plasma via the quasi-Joule dissipation (an enhanced, anomalous resistivity is needed to yield a significant plasma heating), while the fraction of the runaway electrons capable of forming the mentioned seed population, will remain relatively minor.

Let us estimate what DC field  $E$  is required to form the seed populations at the preflare phase. Adopting typical parameters of the preflare source,  $n_{th} \sim 10^{10} \text{ cm}^{-3}$  and  $T \sim 30 \text{ MK}$ , the electron Dreicer field is about  $E_{De} \approx 3 \times 10^{-5} \text{ V/cm}$ . The nonthermal to thermal electron number density ratio is about  $10^{-4}$ . To build this nonthermal

component from the maxwellian tail, electrons with  $v > v_{cr}$  (where  $\exp(-v_{cr}^2/2v_{th}^2) \sim 10^{-4}$ ) must runaway due to the DC electric field. Given that  $v_{cr}^2 \sim (E_{De}/E)v_{th}^2$ , we find  $E \sim 1.5 \times 10^{-6}$  V/cm. Over a typical source size of  $\sim 10^9$  cm, an electron can gain about 1 keV of energy. This energy is far too small compared with the observed electron energies of 1 MeV or above. So this assumed DC field plays no role in forming the nonthermal power-law distribution responsible for nonthermal GS radiation. However, this  $\sim 1$  keV of energy gain can be sufficient enough to form a slightly suprathermal seed population, from which the bulk (presumably stochastic) acceleration produces the observed nonthermal power-law tails up to relativistic energies.

Microwave observations, therefore, show that even the energy release mechanism in the preflare phase, which is almost thermal, is, nevertheless, accompanied by particle acceleration. The nonthermal emission produced by accelerated electrons with energy of several hundred keV to a few MeV appears as early as the soft X-ray emission. The frequency of the spectrum peak is below 10 GHz for the early flare phase of microwave emission in all cases, because of a relatively small number of accelerated electrons at the radio sources. Microwave spectra show that magnetic field in the coronal sources are a few hundred Gauss at the early phase. In some cases the number of accelerated electrons is so low that the gyrosynchrotron emission from *thermal* electrons dominates the low frequency part of the microwave spectrum. The microwave observations of the preflare events are, thus, promising for studying the transitions from the gradual preflare energy release to the flash flare explosives.

## 6. Discussion

The described findings give rise to a number of fundamentally important conclusions about the flare heating and acceleration. (i) The flare energy release is capable of directly heating the thermal plasma, *without* noticeable *in situ* heating by fast electron beams or chromospheric evaporation driven by either electron beams or heat conduction. (ii) The fully developed acceleration process of only a minor fraction of the plasma electrons at the preflare phase implies that the acceleration mechanism involved is inefficient of accelerating electrons directly from the thermal pool, but requires a pre-extracted (injected) seed electron population. (iii) This implies that the electron injection from the thermal pool and their further acceleration toward higher energies are driven by physically distinct processes. The first of them is inefficient or somehow suppressed during the early flare phase, while the second is already fully operational. In contrast, at the impulsive phase this injection process is highly efficient up to another extreme, when all or almost all thermal electrons are accelerated. In particular, the acceleration by cascading turbulence alone seems to be insufficient here. Since in the corresponding acceleration model both injection and acceleration are driven by the same turbulence intensity, so having these broad range of the thermal-to-nonthermal

partitions (from 0 to 100%) while comparably efficient acceleration looks at odds to this acceleration model. (iv) The observed significant plasma heating (in the early flare phases and in 2002 Apr 11 event) suggests that the corresponding flare energy is already available. However, it is divided highly unevenly between the plasma heating and nonthermal population creation. We propose, this is due to yet unspecified energy partition process operating in a way showing some resemblance to that controlling the balance between Joule heating, and runaway electrons in a DC electric field. For a larger DC electric field the fraction of the runaway electrons will grow quickly, resulting in a powerful nonthermal component needed to produce the impulsive flare phase. We emphasize, that in addition to this energy partitioning process, some sort of stochastic acceleration capable of producing the observed power-law electron spectra is still needed during both early and impulsive flare phases.

Properties of the accelerated electron components are somewhat different in the considered 'cold' and 'hot' flares. Firstly, in the 2002 April 11 event the accelerated electron spectrum is noticeably softer ( $\delta \approx 5$ ) than in the cold flares ( $\delta \approx 3.5$ ). Secondly, in the cold, tenuous flare the accelerated electrons are detected at the energies above 6 keV, while in the April 11 event they are only seen above  $\sim 20$  keV; lower-energy X-ray emission is dominated by the thermal background. Thirdly, the acceleration efficiency is different: in the cold, tenuous flare almost all available electrons were accelerated, while in the April 11 event even the peak instantaneous number density of the fast electrons ( $n_r \sim 2 \cdot 10^8 \text{ cm}^{-3}$ ) does not exceed 10% of the thermal electron density. Fourthly, in the April 11 event we clearly see a spectral evolution indicative of the growth of a power-law tail ( $E_{\max}$  increases with time at the acceleration stage), whereas no spectral evolution was detected in the cold, tenuous flare, which implies a nearly instantaneous growth of the power-law tail.

Let us discuss from whence all these differences could originate. We have already concluded that the bulk acceleration mechanism is likely to be a stochastic/Fermi process with a relatively long residence time of the electrons controlled by their spatial diffusion on the turbulent magnetic irregularities at the acceleration region. For a diffusive Fermi acceleration process the shape of the particle energy spectrum depends primarily on the ratio of two key parameters—the acceleration rate  $\tau_a$  (this is the time needed to establish the nonthermal particle spectrum, not to be interpreted as a duration of the acceleration process) and the residence/diffusion time of the electrons  $\tau_d$  at the acceleration region in such a way that the larger the  $\tau_a/\tau_d$  ratio the steeper (softer) the accelerated electron spectrum, (see, e.g., Hamilton & Petrosian 1992). The residence times,  $\tau_d \sim 3$  s, are comparable in the two events under comparison; the acceleration rates are, however, different. Indeed, the acceleration time  $\tau_a$  can be roughly estimated as the time needed for the power-law tail to grow, which is clearly shorter than the residence time,  $\tau_a < 3$  s, in the cold flare (recall, no spectral evolution was noted), while longer,  $\tau_a > 3$  s, in the April 11 event

( $E_{\max}$  increases with time). Thus, for other conditions being equal, the accelerated electron energy spectral index must be larger in the April 11 event in agreement with observations. Note, that the residence time of relativistic electrons in the cold, dense flare is much longer: about 40 s. Interestingly, data on all three flares are consistent with an acceleration process with an energy-independent escape time from the acceleration region.

The acceleration efficiency and energy balance in the flare depend, in addition to the acceleration mechanism itself, on the process of electron extraction from the thermal pool and their injection into the main acceleration process. In the cold flare almost all available thermal electrons were injected and accelerated, although their consequent energy losses were insufficient to significantly heat the thermal plasma. In contrast, in the April 11 event, only a relatively minor fraction of the thermal electrons were accelerated, making the collisional heating of the thermal plasma even less efficient than in the cold flare case (given that other relevant physical parameters are similar in these two cases). Thus, the presence of a very hot flaring SXR plasma with  $T \sim 20$  MK (which is present even before the flare impulsive phase) requires another heating mechanism distinct from the collisional plasma heating by accelerated electrons. This conclusion is further supported by the spatial displacement between the thermal SXR source and nonthermal coronal HXR and microwave sources.

Although the available data are insufficient to firmly identify the flare energization process in the presented events, or the mechanism of energy division between the thermal and nonthermal components, we can conclude that this process does show some resemblance to that controlling the balance between Joule heating and runaway electrons in a DC electric field. Indeed, suppose that there is a relatively weak sub-Dreicer electric field directed along the flaring loop magnetic field. This electric field will initiate an electric current, which will lose its energy through Joule heating, while the fraction of the runaway electrons available for further stochastic acceleration will be relatively minor. In the case of a stronger electric field, e.g., comparable to the Dreicer field, the fraction of the runaway electrons becomes large, while the Joule heating is reduced so the plasma heating is modest. Even though it is a long way from these speculations to even a qualitative model, the analysis performed favors a flare picture in which electrons are first extracted from the thermal pool by a DC electric field (of yet unspecified origin) and then stochastically accelerated to form a power-law-like energy distribution. Therefore, a stochastic acceleration mechanism naturally containing a DC electric field is called for.

One attractive option naturally providing this combination of the stochastic and DC field acceleration is the case of stochastic acceleration by helical turbulence (Fleishman & Toptygin 2013b). Importantly, the turbulence existed on top of a twisted (nonpotential) magnetic field possesses necessarily a nonzero kinetic helicity, which results in a non-zero DC electric field formed by this turbulence. This DC field can efficiently act against the Dreicer field to ex-

tract a runaway fraction of electrons from the thermal pool. This fraction can vary strongly depending on the ratio of this DC field to the Dreicer field, and so can result in any thermal-to-nonthermal energy partition; the runaway electron fraction then supplies the stochastic acceleration process. Having the energy-independent escape time is then consistent with nonresonant stochastic acceleration of the electrons by long-wave turbulence (Bykov & Fleishman 2009; Fleishman & Toptygin 2013a).

Therefore, we have shown that observations of radio emission directly from the acceleration site provide important constraints on the acceleration mechanism in solar flares. Despite the great differences between various flares and the preflare phase, a similar acceleration mechanism, although operating in a somewhat different parameter regimes, seems to be called for. Future radio spectral imaging observations that can better separate the acceleration site from the sites of trapping and precipitation are needed to investigate the flare acceleration mechanism(s) in more detail.

This work was supported in part by NSF grants AGS-0961867, AST-0908344, AGS-1250374 and NASA grants NNX10AF27G and NNX11AB49G to New Jersey Institute of Technology and by the RFBR grants 12-02-00173 and 12-02-00616. This work also benefited from workshop support from the International Space Science Institute (ISSI).

## References

- Altynsev, A. A., Fleishman, G. D., Lesovoi, S. V., & Meshalkina, N. S. 2012, *ApJ*, 758, 138
- Bastian, T. S., Fleishman, G. D., & Gary, D. E. 2007, *ApJ*, 666, 1256
- Battaglia, M., Fletcher, L., & Benz, A. O. 2009, *A&A*, 498, 891
- Bykov, A. M., & Fleishman, G. D. 2009, *ApJL*, 692, L45
- Fleishman, G. D., Kontar, E. P., Nita, G. M., & Gary, D. E. 2011, *ApJL*, 731, L19
- Fleishman, G. D., & Toptygin, I. N. 2013a, *Cosmic Electrodynamics*
- . 2013b, *MNRAS*, 429, 2515
- Hamilton, R. J., & Petrosian, V. 1992, *ApJ*, 398, 350
- Kundu, M. R., White, S. M., Shibasaki, K., Sakurai, T., & Grechnev, V. V. 2001, *ApJ*, 547, 1090
- Lee, J. W., Gary, D. E., & Zirin, H. 1994, *Sol. Phys.*, 152, 409
- Li, Y., & Fleishman, G. D. 2009, *ApJL*, 701, L52
- Melnikov, V. F. 1994, *Radiophysics and Quantum Electronics*, 37, 557
- Melnikov, V. F., Shibasaki, K., & Reznikova, V. E. 2002, *ApJL*, 580, L185
- Park, S., & Fleishman, G. D. 2010, *Sol. Phys.*, 266, 323
- Petrosian, V. 2012, *Space Sci. Rev.*, 49
- Press, W. H., Flannery, B. P., & Teukolsky, S. A. 1986, *Numerical recipes. The art of scientific computing* (Cambridge: University Press, 1986)
- Reznikova, V. E., Melnikov, V. F., Shibasaki, K., Gorbikov, S. P., Pyatakov, N. P., Myagkova, I. N., & Ji, H. 2009, *ApJ*, 697, 735